Hierarchically Porous ZIF-67/Chitosan Beads with High Surface Area and Strengthened Mechanical Properties: Application to CO2 Storage

Nisrine Hammi, Nelly Couzon, Thierry Loiseau, Christophe Volkringer, Abdelkrim El Kadib, Sebastien Royer, Jeremy Dhainaut

Materials Today Sustainability xxx (xxxx) 100394

Contents lists available at ScienceDirect

Materials Today Sustainability

journal homepage: www.elsevier.com

Journal Cover Image

Hierarchically porous ZIF-67/chitosan beads with high surface area and strengthened mechanical properties: Application to CO_2 storage

N. Hammi [a, b, **], N. Couzon [a], T. Loiseau [a], C. Volkringer [a], A. El Kadib [c], S. Royer [a], J. Dhainaut [a, *]

[a] Univ. Lille, CNRS, Centrale Lille, Univ. Artois, UMR 8181 – UCCS – Unité de Catalyse et Chimie du Solide, F-59000, Lille, France
[b] Univ. Lille, CNRS, INRA, Centrale Lille, Univ. Artois, FR 2638 – IMEC – Institut Michel-Eugène Chevreul, 59000, Lille, France
[c] Euromed Research Center, Engineering Division, Euro-Med University of Fes (UEMF), Route de Meknes, Rond-point de Bensouda, 30070, Fès, Morocco

ARTICLE INFO

Article history:
Received 5 January 2023
Received in revised form 23 February 2023
Accepted 26 March 2023

Keywords:
Metal-organic framework
Chitosan beads
Shaping
CO_2 adsorption

ABSTRACT

In this work, zeolitic imidazolate framework-67 (ZIF-67)/chitosan composite beads were prepared by immersing chitosan beads incorporating cobalt (hydr)oxide into a solution containing the organic linker (2-methylimidazole). Compared to the conventional preparation protocols for metal-organic framework/polymer beads, the *in-situ* growth approach developed herein allows obtaining higher surface area with the shaped composites, up to 1200 m^2/g for ZIF-67/$CS_{2:1}$. The CO_2 adsorption capacity of these ZIF-67/chitosan beads was investigated and reached 1.21 mmol/g at 273 K, which represents almost 100% of the adsorption capacity of pure ZIF-67, in line with the preserved surface area despite the incorporation of the 19% of additives included. Importantly, the ZIF-67/chitosan beads with an average bulk (crush) strength of 1.57 N could be easily regenerated, with a retained efficiency above 97% after 6 cycles. Furthermore, a possible mechanism for CO_2 adsorption is discussed.

1. Introduction

The shaping of porous metal-organic frameworks (MOFs) is a vibrant area of research for the development of next-generation adsorption technologies [1]. In this perspective, MOFs have been shaped into various structures, such as membranes [2], foams [3], and monoliths [4]. Recently, the formulation of MOFs into resistant beads has been gaining considerable attention [5]. Various techniques, including extrusion, pressing, and granulation, can be used to process a crystalline powder into beads [6]. However, the mechanical and thermal stability of MOFs, made of metallic nodes coordinated by organic ligands, impose practical limits to the formulation method. For example, the high-temperature treatment under oxidative conditions typically applied with clay binders cannot be used [7]. Besides, the applied pressure on the binder-free MOF powders reduces the interparticular voids, leading to severe amorphization in many cases. For example, several studies on MOF-5 pelletization reported evidences of peak broadening in the powder X-ray diffraction (XRD) patterns as the compression pressure increased, as well as in a largely decreased final Brunauer-Emmett-Teller (BET) surface area (S_{BET}) which was only 6 m^2/g for the pellet compared to 3450 m^2/g for the parent powder [8–10], while the use of binders including natural or synthetic polymers leads to dramatic pore blocking [11]. For instance, HKUST-1 (Hong Kong University of Science and Technology-1) has been shaped following extrusion in the presence of polyvinyl alcohol solution (15 wt%), which greatly affected the resulting porosity, leading to a total loss of surface area of around 45% [12,].

To deal with these issues, a nascent research field where MOF particles are hybridized with other substructures, including synthetic polymers and natural biopolymers, is expected to greatly improve their flexibility, recyclability, and processability [14,15] as well as to further promote their use in industrial technologies with a special emphasis on applications requiring multifunctional and hierarchical porous frameworks, such as adsorption. Cellulose and alginate have been explored as biotemplates to incorporate MOF particles including HKUST-1, ZIF-8, MIL-100(Fe), UiO-66, and ZIF-67 [16,17]. The obtained MOFs-polymer composites display the inherent properties of the two material components. The absence of strong chelating groups in cellulose weakens interfacial interactions with the resulting MOFs, while a significant decrease in the porosity was noticed with the use of alginate. For instance, an alginate-ZIF-8 composite only showed a low surface areas (563 m^2/g) compared to the pristine ZIF-8 (1340 m^2/g) [18–21]. Alternatively, chitosan (CS) presents a better option owing to the presence of amine and acetamide functions in its backbone and the possible swelling of its entangled fibrils when molded as self-standing hydrogel beads [22]. The latter acts as nanoreactors to grow and confine a variety of nano-objects including sol–gel clusters [23], metal nanoparticles [24], lamellar montmorillonite clays [25], exfoliated graphene oxide

* Corresponding author.
** Corresponding author. Univ. Lille, CNRS, Centrale Lille, Univ. Artois, UMR 8181 – UCCS – Unité de Catalyse et Chimie du Solide, F-59000 Lille, France
E-mail addresses: nisrine.hammi@univ-lille.fr (N. Hammi), jeremy.dhainaut@univ-lille.fr (J. Dhainaut).

https://doi.org/10.1016/j.mtsust.2023.100394
2589-2347/© 20XX

sheets [26], and metal centers in MOFs [27]. The combination of MOFs with CS can not only avoid the aforementioned drawbacks but also benefit from both components by obtaining shapeable adsorbents with improved adsorption capacity [28]. According to previous reports, MOF-polymer composites are usually prepared from direct blending or *in-situ* growth [29]. The blending strategy can lead to MOF particles aggregation, and hence materials which are heterogeneous in composition and may suffer from pore blocking. For example, a predefined amount of UiO-66_COOH (72.5 vol%) was mixed with silicon resin and has been shaped following extrusion, which greatly affected the resulting porosity (a S_{BET} loss of 40% with 5.5 wt % of silicon resin) [30]. In contrast, the *in-situ* growth strategy allows the preparation of homogeneous MOF-CS composite adsorbents. However, the latter process is limited by the polymer surface wettability, roughness, and charge properties. Thus, the improvement of the compatibility between MOF particles and polymers remains challenging. Recently, MOFs synthesized from metal hydroxides and metal oxides have been reported [31,32]. In our previous work, we proposed a novel strategy for the *in-situ* growth of microporous MOFs within CS microspheres to form MOF/CS gel beads [33]. Using supercritical drying or freeze-drying techniques, the liquid–vapor interface and capillary pressure are limited so that the ensuing gels are dried into aerogels/cryogels while preserving the original structure, size, and shape [34]. Such beads also present a hierarchical pore network with interconnected micropores, mesopores, and macropores.

Among the MOFs, ZIF-67 has gained a great deal of interest since the original report by Yaghi et al. [35]. High chemical and thermal stability (up to 500 °C), and large surface area (from 595 to 1730 m^2/g) originating from high crystallinity and regular topology structure, make ZIF-67 one of the most appropriate porous materials for the selective capture of CO_2, with adsorption capacities up to 3 mmol/g being reported [36,37]. Although most studies have focused on the shaping of MOFs into mechanically-robust beads, there is no available study on the CO_2 adsorption over structured ZIF-67 beads, even if the processing of this promising MOF phase represents a key to further process developments.

In this work, ZIF-67-based beads with high specific surface areas were prepared by the *in-situ* growth process followed by freeze drying. CS was coordinated with a cobalt salt precursor and subsequently mixed with the 2-methylimidazolate ligand to form ZIF-67@CS composite beads with high MOF loadings, up to 81%, and stable hierarchical microporous/mesoporous/macroporous structures. Benefiting from large surface areas, hierarchical porosities, high dispersions of ZIF-67 crystals in the CS matrix, multiple adsorption sites favorable to CO_2 (–NH– and $–NH_2$ groups, open CO^{2+} sites) and facile recoverability owing to their fair mechanical resistance, ZIF-67@CS beads were subjected to cycles of CO_2 adsorption.

2. Materials and experiments

2.1. Materials

$Co(NO_3)_2{\cdot}6H_2O$, 2-methylimidazole, absolute ethanol, acetic acid (99%), methanol (99.9%), and CS (high molecular weight (viscosity 800–2000 Cp) and deacetylation degree >75%) were purchased from Sigma Aldrich and used without any further purification.

2.2. Synthesis of ZIF-67/CS beads

1.5 g of high molecular weight CS powder was dissolved in 75 mL acetic acid aqueous solution (5 wt%) and stirred for 24 h. Next, a selected mass of $Co(NO_3)_2{\cdot}6H_2O$ with different molar ratio (2:1; 1:1; 1:2) with respect to NH_2 groups (5.8 mmol/g) of CS was added to the transparent solution. The resulting mixture was stirred for an additional 2 h at room temperature until complete homogenization. Following the dropwise addition of this solution into a NaOH bath (4 M), the spontaneous CS gelation into beads was induced. After 5 h of aging in the alkaline solution, the beads were washed with distilled water (1.5 L) until the filtrate approached neutral pH, and then dehydrated for 15 min by successive immersion in a series of ethanol-water baths (10–90, 30–70, 50–50, 70–30, 90–10, 100–0 vol%) [38]. Next, the beads were placed in a polytetrafluoroethylene bottle with screw-on cap, containing a mixture of alcoholic solution and ligand and placed in an oven at 80 °C for 24 h in order to trigger ZIF-67 crystallization. The resulting ZIF-67/CS composite beads were frozen using a mixture of 2-propanol and liquid nitrogen at −82 °C. Lastly, the frozen beads were transferred to the freeze-drier for 1 day. Thus, the cryogel named ZIF-67/$CS_{x:y}$ (x:y corresponding to the molar ratio Co:CS NH_2 groups) was formed.

For comparison, pure CS beads and CS beads with only the metal ($Co/CS_{2:1}$) were also prepared under similar conditions. Besides, in order to study the role of the nitrogen, nitrogen-free polymer beads named ZIF-67/$SA_{2:1}$ were prepared as described in ESI, section S1, using alginate instead of CS.

2.3. Procedure for ZIF-67/CS gas adsorption

Low pressure CO_2-sorption measurements were conducted on a Micromeritics ASAP 2020 system. About 50 mg of sample were loaded in a sample cell and degassed for at least 8 h at 100 °C under secondary vacuum (<5 mmHg) to remove all traces of moisture and pre-adsorbed gases. CO_2 adsorption measurements were conducted at 273 K, while CO_2 desorption was performed at 100 °C under secondary vacuum. Up to 6 adsorption–desorption cycles were conducted over the degassed adsorbents to test their reusability.

2.4. Characterization

N_2-sorption isotherms were recorded at 77K on a Micromeritics Tristar II system. Before analysis, the samples were outgassed under dynamic vacuum at 120 °C overnight. Specific surface area was determined using the multipoint BET algorithm in a p/p_0 range from 0.1 to 0.25 and the total pore volume was measured from the adsorption branch at $P/P_0 = 0.98$. The pore diameters and the pore size distributions were calculated from the desorption branch using the Barrett–Joyner–Halenda and non-local density functional theory methods. A Micromeritics Autopore IV 9500 penetrometer was used to perform mercury intrusion porosimetry. A contact angle of 130° was assumed in the pore size calculations. Powder XRD was performed using a Bruker X-ray AXS D8 Advance diffractometer in Bragg-Brentano configuration and equipped with a LynxEye Super Speed detector. XRD patterns were recorded with Cu Kα radiation ($\lambda = 0.154$ nm, 40 kV, 30 mA) in the 10–80° 2θ range with a 0.02° 2θ step. Phase identification was made by comparison with the ICDD database. Diffuse reflectance infrared Fourier transform spectra were monitored using a NICOLET iS10 spectrometer. Thermogravimetric analysis profiles were obtained using a thermogravimetric analyzer SDT2960 under constant flow of simulated air (20 vol% O_2-80 vol% N_2) from room temperature to 900 °C with a 5 °C/min heating rate. A Vinci Technologies Versatile Crushing Strength Tester was used to perform crushing tests on single solids, using a set of flat anvil and hammer. The load applied was recorded by the force sensor as a function of the displacement of the punch at a constant speed of 0.6 mm/min until failure, happening at the ultimate crushing strength of the solid. For each sample, 10 representative solids were crushed and the resulting values, given in Newton, were averaged. Laser Raman Spectroscopy was performed using a Spectra Physics krypton ion laser at room temperature using the 647.1 nm excitation line. The beam was focused onto the samples using the macroscopic configuration of the apparatus. To avoid damage due to laser heating, all compounds were studied at a very low laser power (3 mW on the sample). Four accumulations were used in each spectral range. No destruction of the material by the laser was observed. The

scattered light was analyzed with an XY Raman Dilor spectrometer equipped with an optical multichannel charge-coupled device liquid nitrogen-cooled detector. The spectral resolution was 0.5 cm^{-1} in the 220–800 cm^{-1} range. Acquisition and data processing were performed with the LABSPEC software. Scanning electronic microscopy (SEM) images were obtained using a JEOL JSM-7800F LV. Inductively coupled plasma–optical emission spectroscopy allowed determining the chemical composition of the composites using the PerkinElmer Optima 2000 DV instrument. A KRATOS Axis Ultra spectrometer operated under ultrahigh vacuum condition, using a twin Al X-ray source (1486.6 eV) at a pass energy of 40 eV, was used for the X-ray photoelectron spectroscopy (XPS) analyses. The solid, in the form of pellet, was fixed on a copper holder with copper tape. The binding energy values were estimated, positioning the C 1s peak of contaminant carbon at a B.E. of 285.0 eV. The Casa XPS software package was used for data analysis.

3. Results and discussion

As illustrated in Fig. 1, ZIF-67/CS beads are prepared starting with the mixing of the aqueous $Co(NO_3)_2{\cdot}6H_2O$ solution and the CS solution, forming Co^{2+}–CS interactions possibly through coordination between the metal ions and the amino groups of CS.

The Co^{2+}–CS complex solution is then added into the NaOH solution to form a $Co(OH)_2$ (or Co_3O_4)–CS alcogel suspension owing to the insolubility of CS in alkali solutions. Afterward, the *in-situ* growth of ZIF-67 crystals along the CS skeleton is triggered by the addition of a solution containing the organic ligand (2-methylimidazole). Finally, the as-prepared alcogel composites are dried by freeze drying, removing the solvent entrapped inside the pores by sublimation. Such dried materials are often called cryogels. It is expected that following direct freeze drying of the alcogel, large macropores would appear as a result of the sublimation of ice crystals, as advantageously used in the freeze-casting approach [39]. However, their presence is detrimental to the resistance of the beads. Thus, gradual solvent exchange with ethanol has been carried out [40]. The resulting ZIF-67/CS cryogels do not show any noticeable damage or structural collapse, as evidenced by the preservation of their diameter during the passage from alcogels to cryogels (Fig. 1).

SEM was used to observe the surface (Fig. 2) and the cross-section (Fig. S1) of the ZIF-67/CS beads. As typically reported, CS-based cryogels are composed of entangled micro-fibrils [41], herein including discrete clusters with the classical rhombic dodecahedron shape attributed to ZIF-67 crystals (Fig. S1), and an average size of 1.3–1.4 μm (Fig. S2). Moreover, Co-based nanoparticles of about 3.9 nm are observed within the beads (Fig. S3). Their presence is attributed to the nitrogen-containing functional groups which inhibit the growth of ZIF-67.

Non-uniform macropores were observed on the surface and in the core of **ZIF-67/$CS_{2:1}$** (Fig. 2b) and **ZIF-67/$CS_{1:1}$** (Fig. 2d). This may be the result of traces of water, which formed ice crystals following the freezing step [39]. Increasing the amount of CS effectively enhanced the coating of MOF crystals as observed within **ZIF-67/$CS_{1:2}$** (Fig. 2f), which is in agreement with a prior study [42]. This indicates that the CS acts both as a structure-directing agent and a surface-coating modifier during the MOF growth and expansion. It is found that the Co, O, and N elements were distributed homogeneously within the cryogels, suggesting the uniform macro-distribution of ZIF-67 crystals inside the beads (Fig. S1).

While powder XRD patterns of pure CS beads (Fig. S4) display only a broad amorphous hump at 20.4° [43], the X-ray diffractogram of **ZIF-67/$CS_{2:1}$** exhibits crystalline peaks that match perfectly the characteristic diffractions of the pristine ZIF-67 (Fig. 3a) [44]. This constitutes salient evidence for the *in-situ* formation of an extended crystalline MOF embedded in CS cryogels. However, when decreasing the Co^{2+}:NH_2 molar ratio (1:1 and 1:2), additional peaks at 2θ values of 19.05° and 38.90° appear and are attributed to [001] and [102] crystalline planes of $Co(OH)_2$ phase (JCPDS: 30–0443) [45]. In particular, **ZIF-67/$CS_{1:2}$** exhibits diffraction peaks attributed to the ZIF-67 phase of low intensity, indicative of a low amount of crystallized ZIF-67. Thus, in the case of CS, the donation discrepancy between the NH_2 of the polysaccharide and the one of the linker, with respect to Co, allows the MOF formation by adjusting the NH_2 to metal ratio. One way to circumvent this issue is by adding more linker to compete with the NH_2 groups of CS. In contrast, the higher interaction strength between alginate and cobalt ions compared to that between the linker (2-methylimidazole) and cobalt ions constitutes a serious impediment for ZIF-67 formation in **ZIF-67/$SA_{2:1}$** [19].

The Fourier transform infrared spectra of ZIF-67/CS composites show the fingerprint of both constituents (Figs. 3b and S5), including the amine band (NH_2) at 1568 cm^{-1} and the carbonyl band (CO–NHMe) at 1650 cm^{-1} of CS [46]. Besides, two characteristic absorption bands of ZIF-67 are observed at 500–800 cm^{-1} and at 1443 cm^{-1}, attributed to the aromatic ring out-of plane bending and methyl bending of 2-methylimidazole, respectively [47]. A substantial decrease of the absorption intensity of –NH_2 and CO–NHMe bands (1570–1640 cm^{-1}) are also noticed, which could be caused by the strong interaction between the cobalt and these N-containing groups. In addition, the absorption band at 485 cm^{-1} is attributed to Co–N stretching, with N coming from either 2-methylimidazole or CS. The presence of the ZIF-67 MOF is also attested from the Raman spectra of the composites, shown in Fig. S6, with peaks at 230–270 cm^{-1} attributed to Co–N bonds, while the signature of imidazole rings is located at around 670 cm^{-1} [48]. As the CS proportion increases, the intensity of Co–N bond decreases, which substantiates the formation of smaller amount of ZIF-67, in consistency with PXRD.

The textural properties of the cryogel composites were evaluated by N_2 sorption and summarized in Table 1. Their resulting surface areas (475–1197 m^2/g) are significantly higher than that of pure CS (72 m^2/g), suggesting that CS does not significantly reduce the accessi-

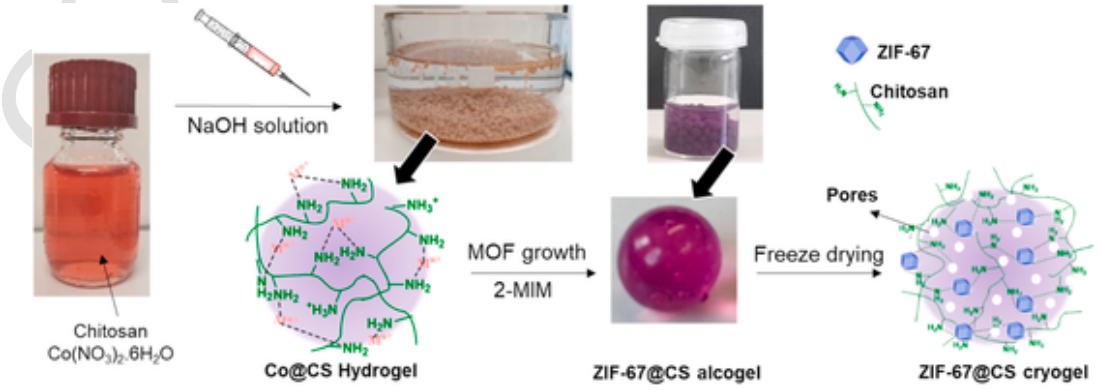

Fig. 1. Illustration of the multistep preparation procedure of ZIF-67/CS beads. CS, chitosan; ZIF, zeolitic imidazolate framework.

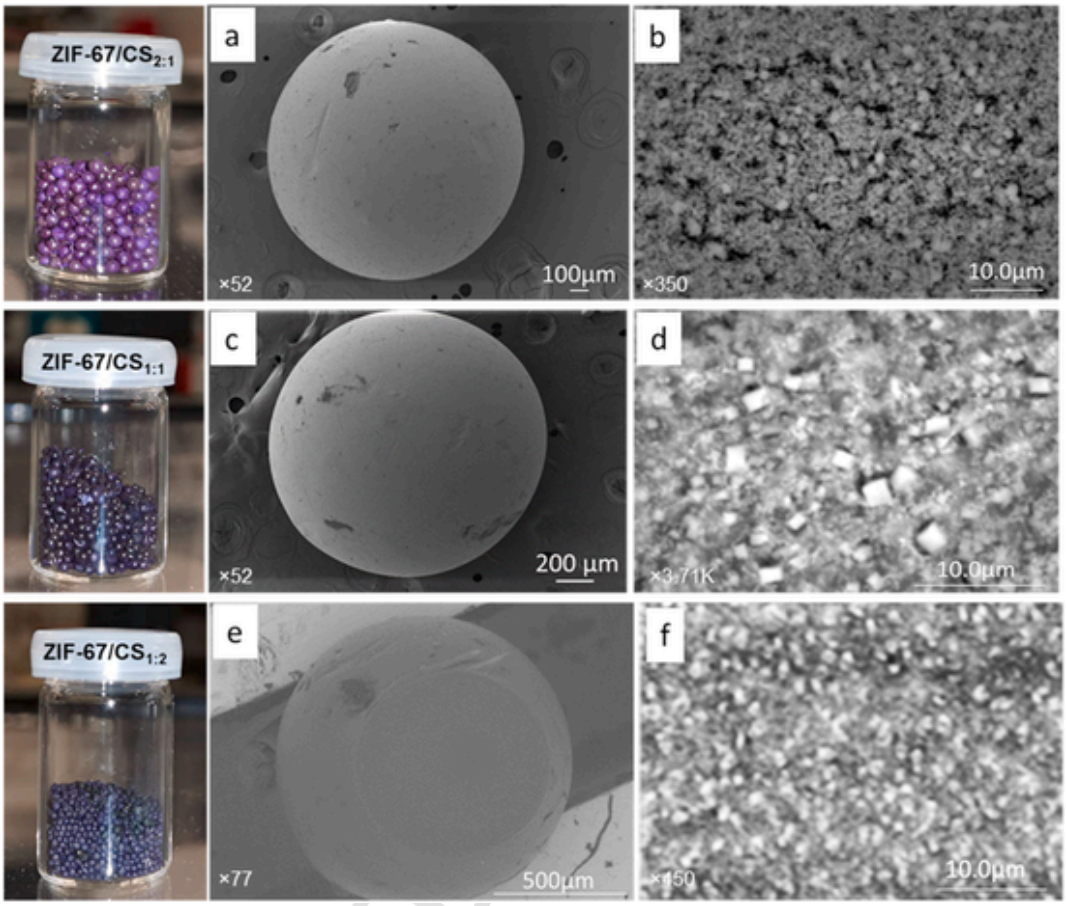

Fig. 2. Digital photos and corresponding SEM images of: **ZIF-67/CS$_{2:1}$** (**a**), (**b**), **ZIF-67/CS$_{1:1}$** (**c**), (**d**) and **ZIF-67/CS$_{1:2}$** (**e**), (**f**). CS, chitosan; SEM, scanning electron microscopy; ZIF, zeolitic imidazolate framework.

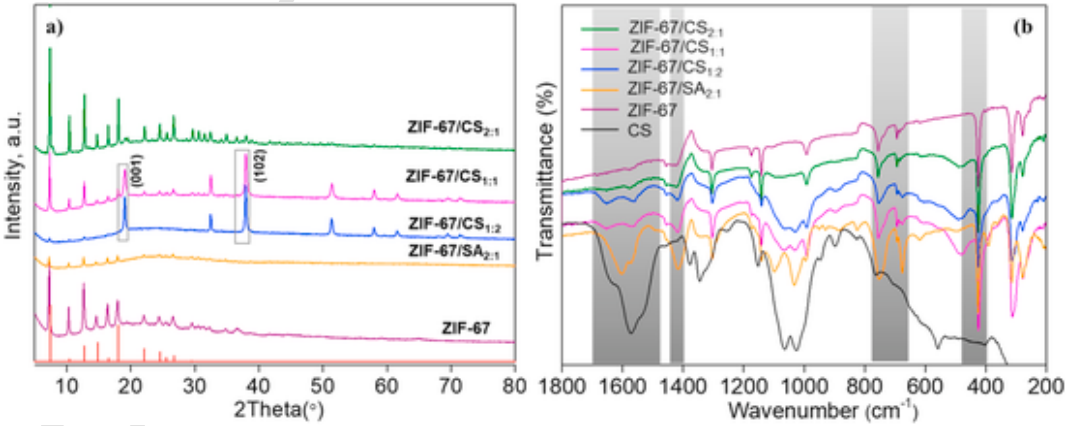

Fig. 3. Powder XRD patterns (**a**) and FTIR spectra (**b**), of **ZIF-67** (experimental and simulated), **ZIF-67/CS$_{2:1}$**, **ZIF-67/CS$_{1:1}$**, **ZIF-67/CS$_{1:2}$**, and **ZIF-67/SA$_{2:1}$**. CS, chitosan; FTIR, Fourier transform infrared; ZIF, zeolitic imidazolate framework.

bility to the surface area of ZIF-67 in dried cryogels. The type I isotherm of the pristine ZIF-67 indicates an expected predominant microporous feature (Fig. S7). On the other hand, all ZIF-67/CS cryogels exhibit hybrid type I–type II isotherms, confirming the retaining of some microporosity in the material with an additional generation of mesopores and macropores due to the entanglement of CS micro-fibrils. In particular, the BET surface area and pore volume of the **ZIF-67/CS$_{2:1}$** are 1197 m^2/g and 0.5 cm^3/g, respectively (Table 1). Besides, its micropore surface area, micropore volume, and the micropore size distribution are 1165 m^2/g, 0.44 cm^3/g, and 1.3/1.5 nm (deduced from non-local density functional theory, Fig. S8), respectively. These values are comparable to the pristine ZIF-67 and in line with the content of MOF inside the cryogels (81%, see hereafter), making it the best result published so far in literature for such materials [49]. However, with the addition of higher contents of CS, the pore volumes and BET surface areas of ZIF-67/CS cryogels decreased significantly in the order: **ZIF-67/CS$_{2:1}$** > **ZIF-67/CS$_{1:1}$**. Indeed, the **ZIF-67/CS$_{2:1}$** composite beads display a lower microporous surface area loss (22%) than that of **ZIF-67/CS$_{1:1}$** (70%), compared to the pristine ZIF-67. A contribution of the CS nanofibrils to the hierarchical porosity can be observed on the pore

Table 1
Textural properties for the ZIF-67/CS beads and the pristine ZIF-67.

Samples	S_{BET} [a] (m^2/g)	S_{μ} [b] (m^2/g)	V_{tot} [c] (cm^3/g)	V_{μ} [d] (cm^3/g)	V_{mes} [e] (cm^3/g)	D_{mes} [g] (nm)
CS	71	–	0.13	–	–	9.6
ZIF-67	1577	1489	0.65	0.57	0.08	–
ZIF-67/$CS_{2:1}$	1197	1165	0.50	0.44	0.06	19.7
ZIF-67/$CS_{1:1}$	475	445	0.27	0.16	0.11	12.8
ZIF-67/$SA_{2:1}$	170	141	0.13	0.05	0.08	43.3
ZIF-67/$CS_{1:2}$	NA	NA	NA	NA	NA	NA
Co/$CS_{2:1}$	NA	NA	NA	NA	NA	NA

f NLDFT pore diameter.
NA: the surface area was too low to be detected accurately.
[a] BET surface area.
[b] Micropore surface area.
[c] Total pore volume obtained at P/Po = 0.98.
[d] Micropore volume with t-plot method.
[e] Mesopore volume determined by subtracting the micropore volume from the total volume.
[g] BJH average pore diameter calculated on desorption branch.

size distribution, with mesopores from 9.6 nm (pure CS) to 12.8–19.7 nm (ZIF-67/CS beads).

Notably, no nitrogen adsorption was detected with **ZIF-67/$CS_{1:2}$**, which reveals that the material is dense or purely macroporous. The lower porosity with increased CS content is attributed to two effects: (i) some of the Co^{2+} failed to be incorporated into ZIF-67. Instead, they partially exist as non-porous $Co(OH)_2$, as indicated by XRD. Also, (ii) there is a possible accumulation of CS around ZIF-67 crystals, partially blocking the porosity. For **ZIF-67/$SA_{2:1}$**, the low textural properties are in line with XRD which showed the formation of a low amount of ZIF-67 crystals, and the presence of randomly distributed free ligands that could interact with the adjacent fibrils through hydrogen bonding, which severely minimize the empty space between the fibrils. Mercury intrusion analysis gives an accurate estimation of the pore size distribution of **ZIF-67/CS** composites beads (Fig. 4a). **ZIF-67/$CS_{2:1}$** and **ZIF-67/$CS_{1:1}$** display a bimodal feature illustrated at the nanopore scale by a relatively broad distribution with peaks centered at 17 nm and 7 nm, respectively, indicating the existence of few mesopores. At the macropores scale, intense contributions are centered at 329 and 310 µm, respectively. Thus, **ZIF-67/$CS_{2:1}$** and **ZIF-67/$CS_{1:1}$** present a multimodal porous structure consisting of interconnected pores ranging from micropores, mesopores to macropores. Such hierarchical porosity presents considerable interests in gas adsorption, with the micropores being associated with the uptake capacity, while the macropores and mesopores improve the adsorption kinetics. On the contrary, **ZIF-67/$CS_{1:2}$** was purely macroporous, with a peak centered at 324 µm.

The thermal stability of these nanocomposites was further assessed using thermogravimetric analysis (Fig. S9). While pure CS microspheres lose their total weight at 580 °C, the composites display a mineral residue varying from 9 wt% to 28 wt% at 800 °C. This residual solid can be attributed to the combustion of ZIF-67, leading to the formation of CoO. According to the structure formula of ZIF-67 ($C_8H_{10}N_4Co$) [33], the ZIF-67 content in ZIF-67/$CS_{2:1}$ can be estimated as 81 wt% (Table S1). This value is in agreement with SEM-energy-dispersive X-ray spectroscopy elemental mapping and inductively coupled plasma–optical emission spectroscopy analyses, based on the metal content (Table S1). The mechanical stability of the resulting ZIF-67/CS beads was also assessed via crushing tests (Figs. 4b and S10). **ZIF-67/$CS_{2:1}$** and **ZIF-67/$CS_{1:1}$** exhibit much higher mechanical resistance than pure CS beads (0.63 ± 0.2 N), giving an average crushing strength of 1.57 ± 0.06 N and 1.48 ± 0.24 N, respectively, while **ZIF-67/$CS_{1:2}$** displays a lower average bulk (crush) strength of 1.26 ± 0.16 N. The results show that the mechanical resistance of these ZIF-67/CS beads is close to the mechanical (crushing) stability of dense UiO-66@HEC granules prepared by Abramova et al. [11] Besides, their mechanical resistance is sufficient for evaluation in CO_2 adsorption.

The final purpose of this work is to highlight the performance of nanostructured ZIF-67/CS cryogel composite beads as adsorbents for CO_2 capture. Fig. 5a shows the CO_2 adsorption isotherms of all the samples at 273 K (100 KPa). A low adsorption capacity of 0.083 mmol·g^{-1} was obtained for the MOF-free sample (**Co/$CS_{2:1}$**), similarly to the pure CS.

After the ZIF-67 *in-situ* growth step, the uptake of **ZIF-67/$CS_{2:1}$** composite beads reached an estimated CO_2 adsorption capacity of 1.21 mmol/g at 100 kPa, similar to the capacity obtained over pristine ZIF-67 (1.23 mmol/g) while its BET surface area is 24% lower (Fig. S11). The CO_2 uptake difference (2%) is in the range of the machine error. This improvement in CO_2 adsorption capacity (per BET surface area) can be attributed to the presence of $–NH_2$ functional groups in CS which provides more CO_2 adsorption sites and increases the affinity toward CO_2. Considering its economic advantage, facility to separate and reuse, and relative mechanical resistance, **ZIF-67/$CS_{2:1}$** shows a great potential for practical CO_2 capture. Further increasing the CS loading in **ZIF-67/$CS_{1:1}$** and **ZIF-67/$CS_{1:2}$** decreased the CO_2 adsorption capacity down to 0.16 mmol/g and 0.05 mmol/g, respectively, which is consis-

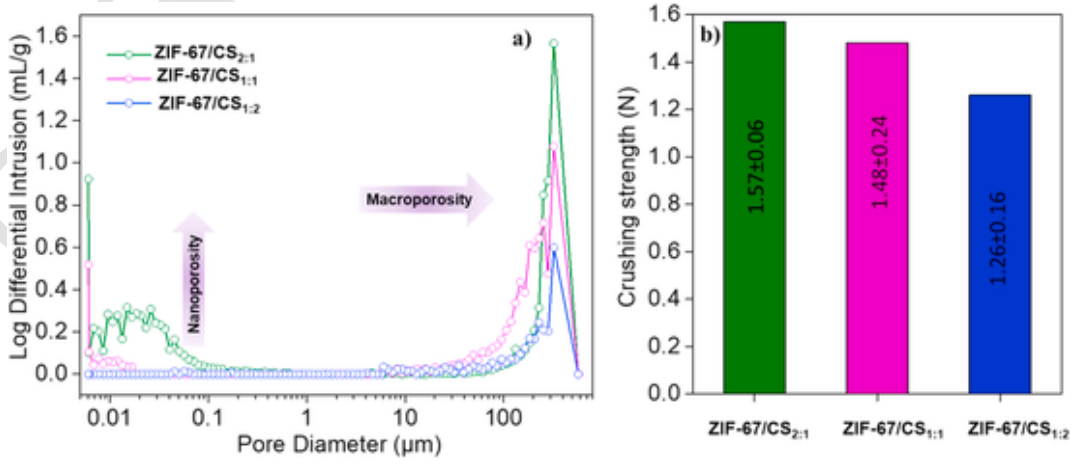

Fig. 4. Pore size distribution estimated by mercury intrusion porosimetry (**a**) and average crushing strength (**b**) of **ZIF-67/$CS_{2:1}$**, **ZIF-67/$CS_{1:1}$**, and **ZIF-67/$CS_{1:2}$**. CS, chitosan; ZIF, zeolitic imidazolate framework.

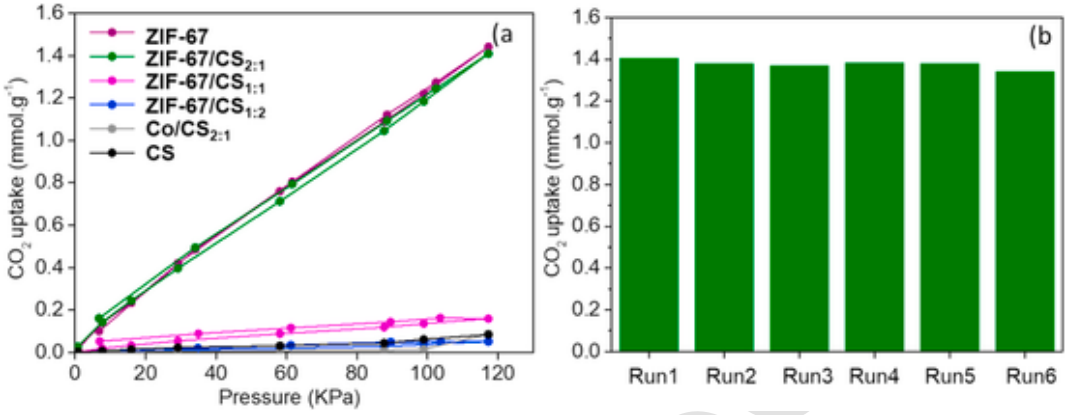

Fig. 5. CO_2 adsorption isotherms of pristine **ZIF-67**, **CS**, **ZIF-67/CS$_{2:1}$**, **ZIF-67/CS$_{1:1}$**, **ZIF-67/CS$_{1:2}$**, **Co/CS$_{2:1}$** and **ZIF-67/SA$_{2:1}$** at 273 K (**a**), cyclical adsorption over **ZIF-67/CS$_{2:1}$** hybrid sorbent at 117 kPa: adsorption at 273 K; desorption at 373 K (**b**). CS, chitosan; ZIF, zeolitic imidazolate framework.

tent with the decreased micropore surface areas (Figs. S11 and S12). This indicates the necessity to maintain a high ZIF-67 content inside the composite beads to ensure high adsorption capacity as the micropore surface contributes significantly to the adsorption process. These results reveal that both the amino functional groups of CS and the textural characteristics of ZIF-67 influence the total CO_2 adsorption capacity. Besides, no significant hysteresis is observed on the CO_2 adsorption–desorption isotherms (Fig. 5a), making them appealing materials for CO_2 sorption cycles.

It is worth to note that the CO_2 adsorption capacities of **ZIF-67/CS$_{2:1}$** reported in this work are remarkably high in comparison to previously reported values (Table 2). The CO_2 uptake of CS/ZIF-8 beads, reported by Li et al. [50], afforded a CO_2 uptake of 3.6 mmol/g at 273 K and 5 bar, but decreased after 3 cycles.

Fig. S13 exhibits the effect of temperature on CO_2 adsorption isotherm. The CO_2 adsorption capacity decreases from 1.21 to 0.76 mmol/g and from 0.16 to 0.12 mmol/g for ZIF-67/CS$_{2:1}$ and ZIF-67/CS$_{1:1}$, respectively, with increasing the operating temperature from 273 to 298 K. This can be explained by the facilitated desorption of CO_2 at elevated temperatures. In order to understand the interaction between CO_2 and ZIF-67/CS composite beads at various temperatures, the isosteric heats of adsorption (Qst) of ZIF-67/CS$_{2:1}$ were calculated using the Clausius–Clapeyron equation based on the CO_2 adsorption isotherms at 273.15 K and 298.15 K (Figs. S14 and S15). Qst for ZIF-67/CS$_{2:1}$ varies in the range of 11.6–44.1 kJ/mol, which is typically ascribed to strong interactions (chemisorption) between CO_2 and cobalt species [51].

Herein, up to 6 cycles of CO_2 adsorption–desorption were carried out over **ZIF-67/CS$_{2:1}$** beads. As shown in Fig. 5b, the **ZIF-67/CS$_{2:1}$** cryogels still exhibit a CO_2 uptake of 1.37 mmol/g, which represents only a minor loss compared to the first cycle (−2%), suggesting the excellent recyclability of ZIF-67/CS$_{2:1}$ for CO_2 uptake, with no damage observed on the beads after multiple cycling, demonstrating that **ZIF-67/CS$_{2:1}$** has good stability during adsorption–desorption cycles. However, after six CO_2-sorption cycles, the powder XRD pattern of **ZIF-67/CS$_{2:1}$** (Fig. S16) shows that the composite is partially degraded as evidenced by the increasing amorphous background, the peak broadening, and the appearance of new peaks (around 19; 31; 38; 51; 58; 62° 2 theta) attributed to $Co(OH)_2$ formation. Besides, the average bulk (crush) strength decreased after 6 cycles (−20%). This may be caused by competitive interaction between CO_2 and 2-methylimidazolate with Co cations.

Table 2
Comparison of the CO_2 and N_2 uptake values reported for various solid adsorbents at different conditions.

Samples	S_{BET} (m^2/g)	Conditions	Uptake (mmol/g)	Refs
CSGO aerogels	33	298 K, 1 bar	0.26	[52]
PI/ZIF composite aerogels	224	298 K, 1 bar	0.4	[53]
MCM-41 + CHIT 50%	424	298 K, 1 bar	0.61	[54]
Chitosan/ZIF-8 composites	268	298 K, 1 bar	0.56	[55]
Chitosan/ZIF-8 beads	99	275 K, 5 bar	3.6	[43]
QCS/PVA aerogels	–	298 K	0.18	[56]
ZIF-67/CS$_{2:1}$ cryogels	1197	298 K, 1 bar	0.76	This work

To date, very few studies have investigated the mechanism of CO_2 adsorption over ZIF-67-based composites. The reaction mechanism may be associated with the nature of the active sites, the surface properties, and the porosity of the adsorbent, and so on [57,58]. A proposed mechanistic pathway for CO_2 adsorption is shown in Scheme 1. **ZIF-67/CS$_{2:1}$** composite beads have a large specific surface area and hierarchical porosity, which is conducive to the efficient adsorption of the CO_2 gas molecules. The main factors which enable **ZIF-67/CS$_{2:1}$** composite beads to adsorb CO_2 could be attributed to the synergy effect of CS modification and ZIF-67 loading, which provides specific interaction sites based on different polar functional groups for CO_2. Infrared characterization was employed to further study the adsorption mechanism of CO_2. No obvious change in IR spectra after the adsorption of CO_2 was observed (Fig. S17), suggesting that there is no chemical interaction between CO_2 and the amino groups of the composite. Especially, there is no characteristic absorbance of carbamate around 1296 and 1414 cm^{-1}, unlike when aqueous amines are used. A physical adsorption process was also reported with other solid adsorbents [59]. XPS analysis was also employed. Before adsorption (Fig. S18a), the high-resolution N 1s spectra of ZIF-67/CS$_{2:1}$ could be fitted to two characteristic peaks at 398.7 eV and 399.9 eV, which represent pyridinic and pyrrolic nitrogens, respectively. After adsorption (Fig. S18b), the binding energy of these two peaks decreased by 1.1 and 1.0 eV, respectively. This finding suggested that CO_2 interacted with –NH groups via hydrogen bond. Moreover, before adsorption, the Co 2p3/2 XPS spectrum can be split into two peaks centered at 781.2 eV and 796.5 eV corresponding to Co 2p3/2 and Co 2p1/2, respectively. The satellite peaks at around 786.1 eV and 802.2 eV highlight the presence of Co(II). After adsorption, the binding energies of Co2p decreased slightly, thereby indicating that the adsorption process also affected the electronic environment around Co atoms. In addition, the high-resolution C 1s spectrum in Fig. S18a can be resolved into three features consistent with C–C, C–N, and C = O at 284.6, 285.9, and 287.0 eV, respectively.

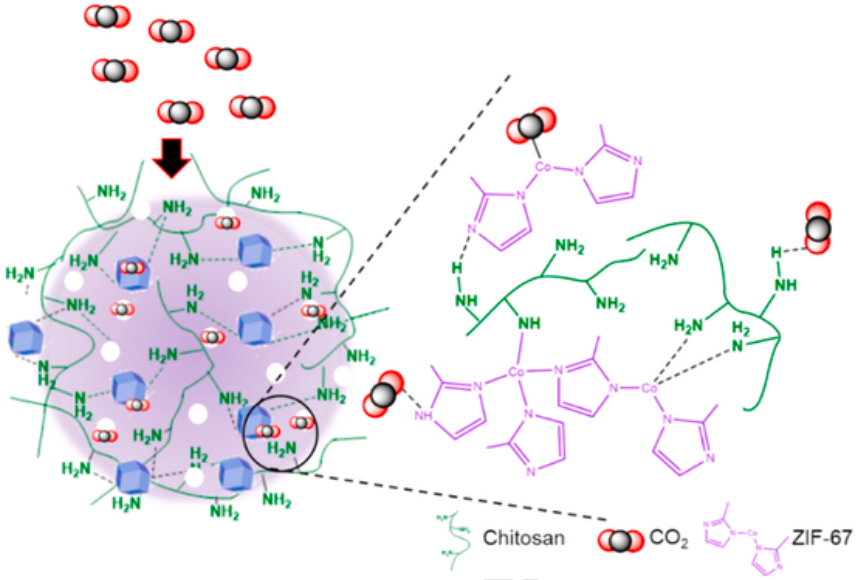

Scheme 1. Proposed adsorption mechanism of CO_2 adsorption on ZIF-67/CS composite beads. CS, chitosan; ZIF, zeolitic imidazolate framework.

Based on the aforementioned characterization results, the CO_2 adsorption mechanism could be discussed. The infrared characterization displayed no chemical interaction between CO_2 and the adsorbent, whereas the XPS characterization demonstrated alterations of the electronic environment of N1 s and Co 2p. The interactions between CO_2 and the adsorbent could thus be reasonably assigned to electrostatic interactions as well as non-chemical hydrogen bonding interactions. In details, on one hand, the unsaturated cobalt centers in ZIF-67 are able to interact with CO_2 [60]. The basic nitrogen sites from the linkers are also beneficial to capture CO_2 via electrostatic interactions [61]. On the other hand, CO_2 can be adsorbed inside the pores of ZIF-67/$CS_{2:1}$ by two types of hydrogen bonding interactions: between CO_2 oxygens and either with the closest hydrogen of the 2-methylimidazole ring or the hydrogen of the amino group present in CS, the latter providing more sites for CO_2 adsorption. These interactions depend on the orientation of CO_2 inside the pores [62,63]. Based on the CO_2 adsorption test results, it can be concluded that hydrogen bonding together with apparent electrostatic interactions may be the possible driving forces for CO_2 adsorption.

4. Conclusion

The synthesis of new ZIF-67/CS composite beads using an *in-situ* growth strategy was demonstrated. The ratio [CS]:[metal] and the experimental conditions affect the formation of the ZIF-67 nanoparticles. The freeze-drying of the soft alcogels resulted in open hierarchical porous frameworks of entangled CS microfibrils holding well-dispersed ZIF-67 crystals. N_2 sorption isotherms corroborated a high surface area (1197 m^2/g) and pore volume for 81 wt% ZIF-67/CS. These results suggested that ZIF-67 particles are well dispersed within the CS matrix, increasing the accessible area. Such loaded cryogels showed a high CO_2 uptake of 1.21 mmol/g at 273 K, which is nearly comparable to that of pristine ZIF-67. In addition, after 6 cycles of CO_2 adsorption–desorption, the cryogels retained more than 97% of their original capacity. Further, the CO_2 adsorption capacities and the stability of **ZIF-67/$CS_{2:1}$** are remarkably high in comparison to the previously reported values in the literature, owing to the multiple adsorption sites present in the composites (Co^{2+} open sites, but also –NH_2 and –NH– groups from CS and 2-MIM linker, respectively).

CRediT author statement

Nisrine Hammi: conceptualization, investigation, writing – original draft. **Nelly Couzon**: investigation. **Thierry Loiseau**: resources, supervision, writing – review & editing. **Christophe Volkringer**: resources, supervision, writing – review & editing. **Abdelkrim El Kadib**: conceptualization, writing – review & editing. **Sébastien Royer**: supervision, funding acquisition, writing – review & editing. **Jérémy Dhainaut**: investigation, supervision, project administration, writing – review & editing.

Declaration of competing interest

The authors declare that they have no known competing financial interests or personal relationships that could have appeared to influence the work reported in this paper.

Data availability

Data will be made available on request.

Acknowledgments

The Chevreul Institute is thanked for its help in the development of this work through the ARCHI-CM project supported by the "Ministere de l'Enseignement Superieur de la Recherche et de l'Innovation", the region "Hauts-de-France", the ERDF program of the European Union and the "Metropole Europeenne de Lille. The region "Hauts-de-France" is also thanked for its support through the REGCAT project. The authors would like to thank Pardis Simon for carrying out X-ray photoelectron spectrometry analysis, Martine Trentesaux for her help with Raman spectroscopy analysis, Laurence Burylo for the powder X-ray diffraction and diffusion facility, Anne-Marie Blanchenet for scanning electron microscopy analyses and Ridvan Yildiz from CERAMATHS laboratory for mercury intrusion.

Appendix A. Supplementary data

Supplementary data to this article can be found online at https://doi.org/10.1016/j.mtsust.2023.100394.

References

[1] H.-C. Zhou, R.J. Long, M.O. Yaghi, Introduction to metal–organic frameworks, Chem. Rev. 112 (2012) 673–674, https://doi.org/10.1021/cr300014x.

[2] S. Qiu, M. Xue, G. Zhu, Metal–organic framework membranes: from synthesis to separation application, Chem. Soc. Rev. 43 (2014) 6116–6140, https://doi.org/10.1039/C4CS00159A.

[3] Y. Chen, X. Huang, S. Zhang, S. Li, S. Cao, X. Pei, J. Zhou, X. Feng, B. Wang, Shaping of metal–organic frameworks: from fluid to shaped bodies and robust foams, J. Am. Chem. Soc. 138 (2016) 10810–10813, https://doi.org/10.1021/jacs.6b06959.

[4] A. Ahmed, M. Forster, R. Clowes, P. Myers, H. Zhang, Hierarchical porous metal–organic framework monoliths, Chem. Commun. 50 (2014) 14314–14316, https://doi.org/10.1039/C4CC06967F.

[5] J. Cousin-Saint-Remi, S. Van der Perre, T. Segato, M.-P. Delplancke, S. Goderis, H. Terryn, G. Baron, J. Denayer, Highly robust MOF polymeric beads with a controllable size for molecular separations, ACS Appl. Mater. Interfaces 11 (2019) 13694–13703, https://doi.org/10.1021/acsami.9b00521.

[6] B. Yeskendir, J.-P. Dacquin, Y. Lorgouilloux, C. Courtois, S. Royer, J. Dhainaut, From metal–organic framework powders to shaped solids: recent developments and challenges, Mater. Adv. 2 (2021) 7139–7186, https://doi.org/10.1039/D1MA00630D.

[7] Y. Liu, Y. Feng, J. Yao, Recent advances in the direct fabrication of millimeter-sized hierarchical porous materials, RSC Adv. 6 (2016) 80840–80846, https://doi.org/10.1039/C6RA17018H.

[8] Y.H. Hu, L. Zhang, Amorphization of metal-organic framework MOF-5 at unusually low applied pressure, Phys. Rev. B 81 (2010) 174103, https://doi.org/10.1103/PhysRevB.81.174103.

[9] Z. Jia, H. Li, Z. Yu, P. Wang, X. Fan, Densification of MOF-5 synthesized at ambient temperature for methane adsorption, Mater. Lett. 65 (2011) 2445–2447, https://doi.org/10.1016/j.matlet.2011.04.099.

[10] D. Bazer-Bachi, L. Assié, V. Lecocq, B. Harbuzaru, V. Falk, Towards industrial use of metal-organic framework: impact of shaping on the MOF properties, Innov. Process. Mater. 255 (2014) 52–59, https://doi.org/10.1016/j.powtec.2013.09.013.

[11] A. Abramova, N. Couzon, M. Leloire, P. Nerisson, L. Cantrel, S. Royer, T. Loiseau, C. Volkringer, J. Dhainaut, Extrusion-spheronization of UiO-66 and UiO-66_NH2 into robust-shaped solids and their use for gaseous molecular iodine, xenon, and krypton adsorption, ACS Appl. Mater. Interfaces 14 (2022) 10669–10680, https://doi.org/10.1021/acsami.1c21380.

[12] J. Kim, S.-H. Kim, S.-T. Yang, W.-S. Ahn, Bench-scale preparation of Cu3(BTC)2 by ethanol reflux: synthesis optimization and adsorption/catalytic applications, Microporous Mesoporous Mater. 161 (2012) 48–55, https://doi.org/10.1016/j.micromeso.2012.05.021.

[13] G. Majano, J. Pérez-Ramírez, Scalable room-temperature conversion of copper (II) hydroxide into HKUST-1 (Cu3(Btc)2), Adv. Mater. 25 (2013) 1052–1057, https://doi.org/10.1002/adma.201203664.

[14] T. Kitao, Y. Zhang, S. Kitagawa, B. Wang, T. Uemura, Hybridization of MOFs and polymers, Chem. Soc. Rev. 46 (2017) 3108–3133, https://doi.org/10.1039/C7CS00041C.

[15] S. El Hankari, M. Bousmina, A. El Kadib, Biopolymer@Metal-Organic framework hybrid materials: a critical survey, Prog. Mater. Sci. 106 (2019) 100579, https://doi.org/10.1016/j.pmatsci.2019.100579.

[16] K. Tu, Y. Ding, T. Keplinger, Review on design strategies and applications of metal-organic framework-cellulose composites, Carbohydr. Polym. 291 (2022) 119539, https://doi.org/10.1016/j.carbpol.2022.119539.

[17] H. Musarurwa, N.T. Tavengwa, Application of polysaccharide-based metal organic framework membranes in separation science, Carbohydr. Polym. 275 (2022) 118743, https://doi.org/10.1016/j.carbpol.2021.118743.

[18] L. Zhu, L. Zong, X. Wu, M. Li, H. Wang, J. You, C. Li, Shapeable fibrous aerogels of metal–organic-frameworks templated with nanocellulose for rapid and large-capacity adsorption, ACS Nano 12 (2018) 4462–4468, https://doi.org/10.1021/acsnano.8b00566.

[19] H. Zhu, Q. Zhang, S. Zhu, Alginate hydrogel: a shapeable and versatile platform for in situ preparation of metal–organic framework–polymer composites, ACS Appl. Mater. Interfaces 8 (2016) 17395–17401, https://doi.org/10.1021/acsami.6b04505.

[20] S. Yang, L. Peng, O.A. Syzgantseva, O. Trukhina, I. Kochetygov, A. Justin, D.T. Sun, H. Abedini, M.A. Syzgantseva, E. Oveisi, G. Lu, W.L. Queen, Preparation of highly porous metal–organic framework beads for metal extraction from liquid streams, J. Am. Chem. Soc. 142 (2020) 13415–13425, https://doi.org/10.1021/jacs.0c02371.

[21] H. Nasser Abdelhamid, L. Valencia, Nanocellulose leaf-like zeolitic imidazolate framework (ZIF-L) foams for selective capture of carbon dioxide, Carbohydr. Polym. 213 (2019) 338–345, https://doi.org/10.1016/j.carbpol.2019.03.011.

[22] A. El Kadib, Green and functional aerogels by macromolecular and textural engineering of chitosan microspheres, Chem. Rec. 20 (2020) 753–772, https://doi.org/10.1002/tcr.201900089.

[23] N. Hammi, N. Wrońska, N. Katir, K. Lisowska, N. Marcotte, T. Cacciaguerra, M. Bryszewska, A. El Kadib, Supramolecular chemistry-driven preparation of nanostructured, transformable, and biologically active chitosan-clustered single, binary, and ternary metal oxide bioplastics, ACS Appl. Bio Mater. 2 (2019) 61–69, https://doi.org/10.1021/acsabm.8b00306.

[24] A. Primo, F. Quignard, Chitosan as efficient porous support for dispersion of highly active gold nanoparticles: design of hybrid catalyst for carbon–carbon bond formation, Chem. Commun. 46 (2010) 5593–5595, https://doi.org/10.1039/C0CC01137A.

[25] S. Frindy, A. Primo, A. el kacem Qaiss, R. Bouhfid, M. Lahcini, H. Garcia, M. Bousmina, A. El Kadib, Insightful understanding of the role of clay topology on the stability of biomimetic hybrid chitosan-clay thin films and CO2-dried porous aerogel microspheres, Carbohydr. Polym. 146 (2016) 353–361, https://doi.org/10.1016/j.carbpol.2016.03.077.

[26] S. Frindy, A. Primo, H. Ennajih, Q.A. el kacem, R. Bouhfid, M. Lahcini, E.M. Essassi, H. Garcia, A. El Kadib, Chitosan–graphene oxide films and CO2-dried porous aerogel microspheres: interfacial interplay and stability, Carbohydr. Polym. 167 (2017) 297–305, https://doi.org/10.1016/j.carbpol.2017.03.034.

[27] H. Musarurwa, N.T. Tavengwa, Advances in the application of chitosan-based metal organic frameworks as adsorbents for environmental remediation, Carbohydr. Polym. 283 (2022) 119153, https://doi.org/10.1016/j.carbpol.2022.119153.

[28] R. Zhao, T. Ma, S. Zhao, H. Rong, Y. Tian, G. Zhu, Uniform and stable immobilization of metal-organic frameworks into chitosan matrix for enhanced tetracycline removal from water, Chem. Eng. J. 382 (2020) 122893, https://doi.org/10.1016/j.cej.2019.122893.

[29] X. Ma, Y. Chai, P. Li, B. Wang, Metal–organic framework films and their potential applications in environmental pollution control, Acc. Chem. Res. 52 (2019) 1461–1470, https://doi.org/10.1021/acs.accounts.9b00113.

[30] Y. Khabzina, J. Dhainaut, M. Ahlhelm, H.-J. Richter, H. Reinsch, N. Stock, D. Farrusseng, Synthesis and shaping scale-up study of functionalized UiO-66 MOF for ammonia air purification filters, Ind. Eng. Chem. Res. 57 (2018) 8200–8208, https://doi.org/10.1021/acs.iecr.8b00808.

[31] F. Wang, S. Jia, D. Li, B. Yu, L. Zhang, Y. Liu, X. Han, R. Zhang, S. Wu, Self-template synthesis of CuO@Cu3(BTC)2 composite and its application in cumene oxidation, Mater. Lett. 164 (2016) 72–75, https://doi.org/10.1016/j.matlet.2015.09.044.

[32] W. Xu, G. Li, W. Li, H. Zhang, Facile room temperature synthesis of metal–organic frameworks from newly synthesized copper/zinc hydroxide and their application in adsorptive desulfurization, RSC Adv. 6 (2016) 37530–37534, https://doi.org/10.1039/C6RA04465D.

[33] N. Hammi, S. Chen, A. Primo, S. Royer, H. Garcia, A. El Kadib, Shaping MOF oxime oxidation catalysts as three-dimensional porous aerogels through structure-directing growth inside chitosan microspheres, Green Chem. 24 (2022) 4533–4543, https://doi.org/10.1039/D2GC00097K.

[34] H.J. Park, D.-W. Lim, W.S. Yang, T.-R. Oh, M.P. Suh, A highly porous metal–organic framework: structural transformations of a guest-free MOF depending on activation method and temperature, Chem. Eur. J. 17 (2011) 7251–7260, https://doi.org/10.1002/chem.201003376.

[35] A. Phan, C.J. Doonan, F.J. Uribe-Romo, C.B. Knobler, M. O'Keeffe, O.M. Yaghi, Synthesis, structure, and carbon dioxide capture properties of zeolitic imidazolate frameworks, Acc. Chem. Res. 43 (2010) 58–67, https://doi.org/10.1021/ar900116g.

[36] W. Li, A. Zhang, X. Jiang, C. Chen, Z. Liu, C. Song, X. Guo, Low temperature CO2 methanation: ZIF-67-Derived Co-based porous carbon catalysts with controlled crystal morphology and size, ACS Sustain. Chem. Eng. 5 (2017) 7824–7831, https://doi.org/10.1021/acssuschemeng.7b01306.

[37] H.N. Abdelhamid, Removal of carbon dioxide using zeolitic imidazolate frameworks: adsorption and conversion via catalysis, Appl. Organomet. Chem. 36 (2022) e6753, https://doi.org/10.1002/aoc.6753.

[38] R. Valentin, K. Molvinger, F. Quignard, D. Brunel, Supercritical CO2 dried chitosan: an efficient intrinsic heterogeneous catalyst in fine chemistry, New J. Chem. 27 (2003) 1690–1692, https://doi.org/10.1039/B310109F.

[39] L. Ma, A. Jin, Z. Xie, W. Lin, Freeze drying significantly increases permanent porosity and hydrogen uptake in 4,4-connected metal–organic frameworks, Angew. Chem. Int. Ed. 48 (2009) 9905–9908, https://doi.org/10.1002/anie.200904983.

[40] D. Chen, H. Gao, P. Liu, P. Huang, X. Huang, Directly ambient pressure dried robust bridged silsesquioxane and methylsiloxane aerogels: effects of precursors and solvents, RSC Adv. 9 (2019) 8664–8671, https://doi.org/10.1039/C8RA08646J.

[41] S. Takeshita, S. Yoda, Chitosan aerogels: transparent, flexible thermal insulators, Chem. Mater. 27 (2015) 7569–7572, https://doi.org/10.1021/acs.chemmater.5b03610.

[42] N. Hammi, S. El Hankari, N. Katir, N. Marcotte, K. Draoui, S. Royer, A. El Kadib, Polysaccharide templated biomimetic growth of hierarchically porous metal-organic frameworks, Microporous Mesoporous Mater. 306 (2020) 110429, https://doi.org/10.1016/j.micromeso.2020.110429.

[43] L. Li, S. Han, S. Zhao, X. Li, B. Liu, Y. Liu, Chitosan modified metal–organic frameworks as a promising carrier for oral drug delivery, RSC Adv. 10 (2020) 45130–45138, https://doi.org/10.1039/D0RA08459J.

[44] J. Cao, C. Lei, J. Yang, X. Cheng, Z. Li, B. Yang, X. Zhang, L. Lei, Y. Hou, K. Ostrikov, An ultrathin cobalt-based zeolitic imidazolate framework nanosheet array with a strong synergistic effect towards the efficient oxygen evolution reaction, J. Mater. Chem. A 6 (2018) 18877–18883, https://doi.org/10.1039/C8TA08337A.

[45] Z. Li, X. Zhang, Y. Kang, C.C. Yu, Y. Wen, M. Hu, D. Meng, W. Song, Y. Yang, Interface engineering of Co-LDH@MOF heterojunction in highly stable and efficient oxygen evolution reaction, Adv. Sci. 8 (2021) 2002631, https://doi.org/10.1002/advs.202002631.

[46] A.E. Kadib, K. Molvinger, M. Bousmina, D. Brunel, Decoration of chitosan microspheres with inorganic oxide clusters: rational design of hierarchically porous, stable and cooperative acid–base nanoreactors, J. Catal. 273 (2010) 147–155, https://doi.org/10.1016/j.jcat.2010.05.010.

[47] S. Fazlifard, T. Mohammadi, O. Bakhtiari, Chitosan/ZIF-8 mixed-matrix membranes for pervaporation dehydration of isopropanol, Chem. Eng. Technol. 40 (2017) 648–655, https://doi.org/10.1002/ceat.201500499.

[48] M. Wang, J. Liu, C. Guo, X. Gao, C. Gong, Y. Wang, B. Liu, X. Li, G.G. Gurzadyan, L. Sun, Metal–organic frameworks (ZIF-67) as efficient cocatalysts for photocatalytic reduction of CO2: the role of the morphology effect, J. Mater. Chem. A 6 (2018) 4768–4775, https://doi.org/10.1039/C8TA00154E.

[49] X. Qian, Q. Ren, X. Wu, J. Sun, H. Wu, J. Lei, Enhanced water stability in Zn-doped zeolitic imidazolate framework-67 (ZIF-67) for CO2 capture applications, ChemistrySelect 3 (2018) 657–661, https://doi.org/10.1002/slct.201702114.

[50] C. Li, N. He, X. Zhao, X. Zhang, W. Li, X. Zhao, Y. Qiao, Chitosan/ZIF-8 composite beads fabricated by in situ growth of MOFs crystals on chitosan beads for CO2 adsorption, ChemistrySelect 7 (2022) e202103927, https://doi.org/10.1002/slct.202103927.

[51] A.A. Alhwaige, T. Agag, H. Ishida, S. Qutubuddin, Biobased chitosan hybrid aerogels with superior adsorption: role of graphene oxide in CO2 capture, RSC Adv. 3 (2013) 16011–16020, https://doi.org/10.1039/C3RA42022A.

[52] N. Hsan, P.K. Dutta, S. Kumar, R. Bera, N. Das, Chitosan grafted graphene oxide aerogel: synthesis, characterization and carbon dioxide capture study, Int. J. Biol. Macromol. 125 (2019) 300–306, https://doi.org/10.1016/j.ijbiomac.2018.12.071.

[53] T. Wu, J. Dong, K. De France, P. Zhang, X. Zhao, Q. Zhang, Porous carbon frameworks with high CO2 capture capacity derived from hierarchical polyimide/zeolitic imidazolate frameworks composite aerogels, Chem. Eng. J. 395 (2020) 124927, https://doi.org/10.1016/j.cej.2020.124927.

[54] D.E.F. Oliveira, J.A.O. Chagas, A.L. de Lima, C.J.A. Mota, CO2 capture over MCM-41 and SBA-15 mesoporous silicas impregnated with chitosan, Ind. Eng. Chem. Res. 61 (2022) 10522–10530, https://doi.org/10.1021/acs.iecr.2c00385.

[55] J. Yao, R. Chen, K. Wang, H. Wang, Direct synthesis of zeolitic imidazolate framework-8/chitosan composites in chitosan hydrogels, Microporous Mesoporous Mater. 165 (2013) 200–204, https://doi.org/10.1016/j.micromeso.2012.08.018.

[56] J. Song, J. Liu, W. Zhao, Y. Chen, H. Xiao, X. Shi, Y. Liu, X. Chen, Quaternized chitosan/PVA aerogels for reversible CO2 capture from ambient air, Ind. Eng. Chem. Res. 57 (2018) 4941–4948, https://doi.org/10.1021/acs.iecr.8b00064.

[57] B. Petrovic, M. Gorbounov, S. Masoudi Soltani, Influence of surface modification on selective CO2 adsorption: a technical review on mechanisms and methods, Microporous Mesoporous Mater. 312 (2021) 110751, https://doi.org/10.1016/j.micromeso.2020.110751.

[58] R. Borgohain, U. Pattnaik, B. Prasad, B. Mandal, A review on chitosan-based membranes for sustainable CO2 separation applications: mechanism, issues, and the way forward, Carbohydr. Polym. 267 (2021) 118178, https://doi.org/10.1016/j.carbpol.2021.118178.

[59] C. Yang, T. Zhao, H. Pan, F. Liu, J. Cao, Q. Lin, Facile preparation of N-doped porous carbon from chitosan and NaNH2 for CO2 adsorption and conversion, Chem. Eng. J. 432 (2022) 134347, https://doi.org/10.1016/j.cej.2021.134347.

[60] Y. Pan, H. Li, X.-X. Zhang, Z. Zhang, X.-S. Tong, C.-Z. Jia, B. Liu, C.-Y. Sun, L.-Y. Yang, G.-J. Chen, Large-scale synthesis of ZIF-67 and highly efficient carbon capture using a ZIF-67/glycol-2-methylimidazole slurry, Chem. Eng. Sci. 137 (2015) 504–514, https://doi.org/10.1016/j.ces.2015.06.069.

[61] R. Dahmani, S. Grubišić, I. Djordjević, S. Ben Yaghlane, S. Boughdiri, G. Chambaud, M. Hochlaf, Silico design of a new Zn–triazole based metal–organic framework for CO2 and H2O adsorption, J. Chem. Phys. 154 (2021) 024303, https://doi.org/10.1063/5.0037594.

[62] Y.G. Ko, S.S. Shin, U.S. Choi, Primary, secondary, and tertiary amines for CO2 capture: designing for mesoporous CO2 adsorbents, J. Colloid Interface Sci. 361 (2011) 594–602, https://doi.org/10.1016/j.jcis.2011.03.045.

[63] Y. Wu, Y. Zhang, N. Chen, S. Dai, H. Jiang, S. Wang, Effects of amine loading on the properties of cellulose nanofibrils aerogel and its CO2 capturing performance, Carbohydr. Polym. 194 (2018) 252–259, https://doi.org/10.1016/j.carbpol.2018.04.017.